169 An investigation of the tornadic stage of the Goshen County, Wyoming, supercell of 5 June 2009 using EnKF assimilation of mobile radar data collected during VORTEX2

JAMES MARQUIS*, YVETTE RICHARDSON, PAUL MARKOWSKI,
Department of Meteorology, Pennsylvania State University, University Park, PA
DAVID DOWELL,
NOAA Earth System Research Laboratory, Boulder, CO
JOSHUA WURMAN, KAREN KOSIBA, AND PAUL ROBINSON
Center for Severe Weather Research, Boulder, CO

1. Introduction

The Goshen County, Wyoming, supercell of 5 June 2009 (hereafter, the Goshen County storm), targeted by the second Verification of the Origins of Rotation in Tornadoes Experiment (VORTEX2; Wurman et al. 2012), is likely the most thoroughly observed tornadic supercell in history. The Doppler on Wheels radars (hereafter DOWs; Wurman et al. 1997), the NSSL NOXP radar (Palmer et al. 2009), mobile mesonets (Straka et al. 1996; Waugh and Fredrickson 2010), and other instruments collected wind data throughout the storm and thermodynamic data near the ground during the intercept of the Goshen County tornado. These observations provide a knowledge of many fine-scale processes playing roles in the generation, maintenance, and decay of near-surface vorticity (Markowski et al. 2012a,b; Kosiba et al. 2012; Richardson et al. 2012). However, despite the large quantity of dual-Doppler and in situ observations collected in the Goshen County supercell, the relatively small size of the dual-Doppler lobes and general lack of velocity observations outside of precipitating regions of the storm precludes a more complete understanding of how the low-level mesocyclone and tornado interact with more distant features of the storm. For example, we cannot confidently comment on the deep vertical structure of the mesocyclone, updrafts, and downdrafts, which may be important for the diagnosis of processes relating to tornado behavior (e.g., Markowski 2002; Dowell and Bluestein 2002; Marquis et al. 2012), with the dual-Doppler observations. Knowledge of the origins of air entering the mesocyclone during certain periods of the tornado life cycle is precluded owing to the curtailed length of trajectories when they reach the edges of the dual-Doppler coverage. Furthermore, errors in the trajectory calculations are introduced by the need to extrapolate velocity data below the radar horizon in the dual-Doppler syntheses (located 100-300 m above ground level in this case). Mobile mesonet observations were collected only within 2 m of the ground, with horizontal coverage dictated by the network of passable roads. A thermodynamic field of greater horizontal extent and depth is needed to gain a thorough understanding of the storm-scale processes influencing tornado formation and maintenance.

Corresponding author address: James Marquis, Department of Meteorology, Pennsylvania State University, 503 Walker Building, University Park, PA 16802; *e-mail*: jnm128@psu.edu.

In this study, we follow a similar methodology to Marquis et al. (2012) to produce ensemble-mean EnKF kinematic and thermodynamic analyses by assimilating observations from various mobile radars deployed during the Goshen County storm into a cloud model. A full description of the model and data assimilation parameters, as well as verification of the EnKF analyses will be presented in an upcoming journal article. The primary focus of this paper is to examine a more complete evolution and structure of certain storm-scale and mesocyclone-scale processes relating to tornado formation, maintenance, and decay than is possible with only the high-resolution dual-Doppler and in situ observations.

2. Method

An ensemble of 50 storms is simulated using the WRF-ARW model version 3.2.1 (Skamarock et al. 2008). We use a horizontal grid spacing of 500 m, a stretched vertical grid with $\Delta z \sim$ 80 m near the ground and $\sim$ 2 km near the top of the domain (20 km ASL), and a large time step of 2 s. We use the Lin et al. (1983) ice microphysics scheme with a graupel density of 900 kg m^{-3} and a Marshall-Palmer intercept parameter of 4×10^3 m^{-4}. Our idealized modeling strategy, owing to computational constraints, assumes flat terrain, no surface fluxes, and no radiative transfer. We use open lateral boundary conditions and implement a Rayleigh damping layer in the uppermost 5 km of the domain. The horizontally homogeneous environment is derived from a NSSL mobile sounding located approximately 50 km south-southeast of the updraft near the time of tornadogenesis (2155 UTC). The boundary-layer temperature and dewpoint profile is modified so that the surface temperature is consistent with mobile mesonet observations in the near-storm inflow environment (Fig 1). Convective updrafts are initiated in each ensemble member 10 min before data assimilation using a random configuration of 10 overlapping warm bubbles placed in an area occupied by the storm. Ensemble spread is maintained throughout the experiments using an additive noise procedure outlined in Dowell and Wicker (2009), with T, T_d, u, and v perturbations of magnitudes 0.25 K and 0.5 m s^{-1} added every 5 minutes to the model fields in areas where radar reflectivity exceeds 25 dBZ_e starting 20 minutes after the start of each experiment (0.8 K and 0.8 m s^{-1} are used prior to this time).

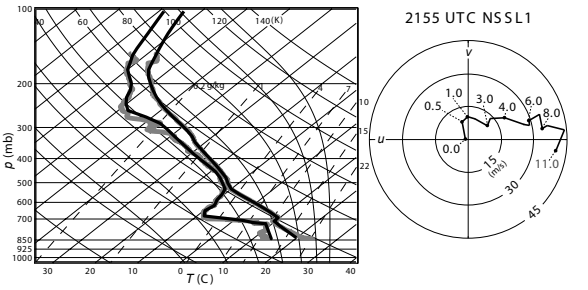

FIG. 1. Skew-T log-P diagram and hodograph of the NSSL1 2155 UTC sounding representing the homogeneous base state in the EnKF experiments. The black lines are the temperature and dewpoint temperature profiles modified with surface mobile mesonet temperature observations. The gray profile illustrates the unmodified boundary layer temperature profile. Various heights along the hodograph are labeled in kilometers.

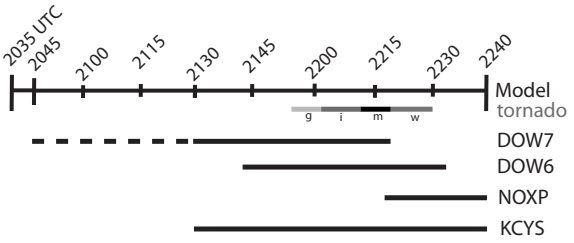

FIG. 2. Timeline of the experiment including model duration, the tornado life cycle (periods of tornadogenesis, intensification, maturity, and weakening are labeled with 'g', 'i', 'm', and 'w', respectively), and the DOW7, DOW6, NOXP, and WSR-88D data assimilation periods. The dashed line represents the period of synthetic DOW7 data.

Data assimilation is performed with the NCAR Data Assimilation Research Testbed (Anderson et al. 2009) software. Figure 2 shows the temporal coverage of the observations assimilated. Data are assimilated at 2-min intervals over a 2-hr period. Only velocity observations are assimilated (reflectivity observations are not assimilated). From 2045–2130 UTC, synthetic radar data, generated by translating the data in the first DOW7 radar volume (valid at 2130 UTC) to their fictitious prior locations consistent with an average storm motion, are assimilated every 2 minutes. These synthetic data are assimilated because the high spatial resolution achieved by DOW7 appears to aid in spinning-up a storm more rapidly than WSR-88D data alone during this period. Prior to assimilation, radar radial velocities are objectively analyzed to positions along their original conical surfaces with a regular horizontal grid spacing of 500 m using a Cressman weighting with a 500-m radius of influence. Only 50% of the objectively analyzed observations are assimilated (every-other observation on the x and y grids) owing to the computational cost of assimilating a large quantity of observations.

3. Near-surface characteristics of the storm

The evolution of the low-level features of the storm surrounding the tornado throughout its life cycle as depicted by EnKF ensemble mean analyses (all analyses herein are derived from ensemble mean EnKF analyses directly following data assimilation; i.e., posterior analyses) is shown in Fig 3. A relatively weak pre-tornadic mesocyclone is found at 2149 UTC near the occlusion point of the forward-flank and rear-flank gust fronts (Fig 3a). The low-level rear-flank downdraft (RFD) located approximately 4 km west of the vorticity maximum is disorganized relative to later times. During the period of tornadogenesis (Fig 3b) the vertical vorticity within the mesocyclone increases substantially, the initial downdraft maximum organizes into an elliptical shape west of the vortex center while a second maximum of downdraft forms just east of the mesocyclone. A band of updraft develops a few km south-southwest of the vorticity maximum within the outflow air. This band resembles a secondary gust front as seen in the high-resolution observations of this storm (Kosiba et al. 2012) and other tornadic storms (e.g., Wurman et al. 2010; Finley et al. 2010; Marquis et al. 2012). During the period of tornado intensification and maturity, the outflow and gust front structure remains fairly constant except that the magnitude of the RFD increases just south and west of the tornado and the outflow temperature becomes much colder north of the tornado. The outflow air continues to get colder and the RFD gets larger in horizontal extent near the mesocyclone after about 2221 UTC (e.g., Fig 3e) such that the pattern of updraft and downdraft spiraling around the vorticity maximum is disrupted. Subsequently, the low-level vorticity maximum dissipates surrounded by weak downdraft and orphaned from the updraft along the gust front (Fig 3f). This evolution of low-level features is qualitatively consistent with descriptions of supercell evolution (e.g., Lemon and Doswell 1979).

The updraft is vertically erect between the surface and midlevels throughout the life cycle of the tornado, though the tilt of the vertical vorticity maximum associated with the mesocyclone varies with time (Fig 4). The mesocyclone is most horizontally tilted during the pre-tornadic/tornadogenesis periods and during the weakening of the tornado (Fig 4a,d), and is the least tilted during tornado intensification and maturity (Fig 4b,c). The low-level vorticity maximum remains underneath the southwestern edge of the midlevel updraft through most of the life cycle of the tornado, except during its final few minutes, when the vertical vorticity maximum below 3 km moves southwestward relative to the main updraft(Fig 4d). The southeast-northwest-oriented horizontal tilt of the mesocyclone below 3 km is consistent with the strong westerly surging outflow winds at low levels on the rear-flank of the storm during this time.

Figure 5a shows the evolution of the near-surface circulation ($\Gamma = \oint \mathbf{v} \cdot \mathbf{dl}$) about a vertical axis centered on the vertical vorticity maximum and azimuthally-averaged radial velocity (relative to the axis of rotation) calculated along rings of various radii throughout the life cycle of the tornado. During the pre-tornadic and tornadogenesis period, low-level circulation increases quite rapidly, and strong (albeit decreasing) radial convergence is present at $r > 1$ km. At these same spatial scales, circulation decreases shortly after tornadogenesis and radial inflow becomes outflow during the end of the intensification phase of the tornado. At small radii ($r < 1$ km), circulation and convergence are steady from 2154–2217 UTC but decrease throughout tornado dissipation. Therefore, tornado formation and maintenance in this case are correlated with radial low-

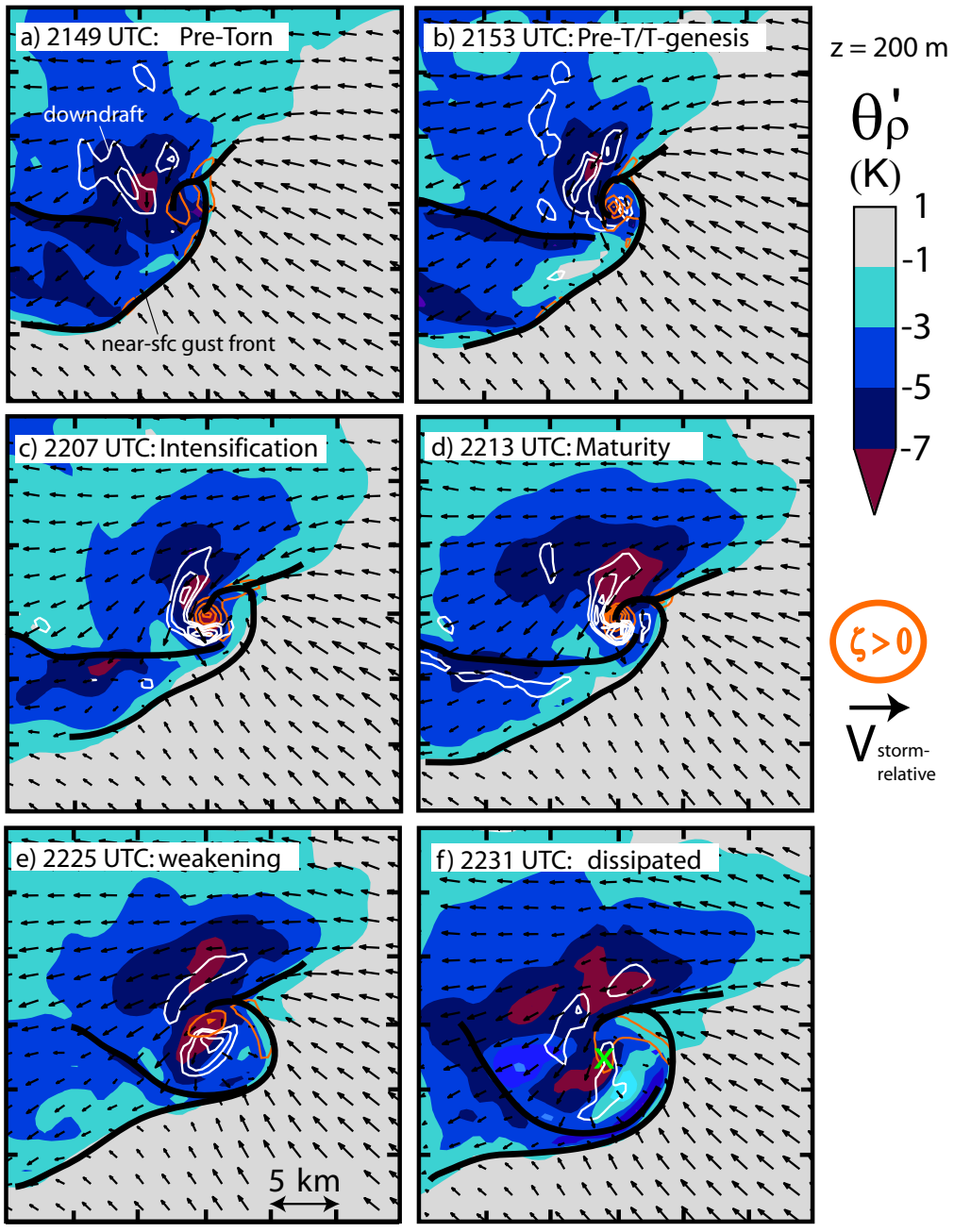

FIG. 3. Ensemble-mean density potential temperature deficit from the environment (shaded), storm-relative horizontal wind (vectors), downdraft (white contours; outermost contour is -0.75 m s^{-1}, incremented by -0.75 m s^{-1}), and positive vertical vorticity (orange contours; outermost contour is 0.01 s^{-1}, incremented by 0.01 s^{-1}) at z = 200 m at six times throughout the life cycle of the tornado. Vertical velocity maxima along the near-surface gust fronts are traced with bold black lines. The 'X' in panel f indicates the location of the remnant vorticity maximum associated with the dissipating tornado-containing mesocyclone.

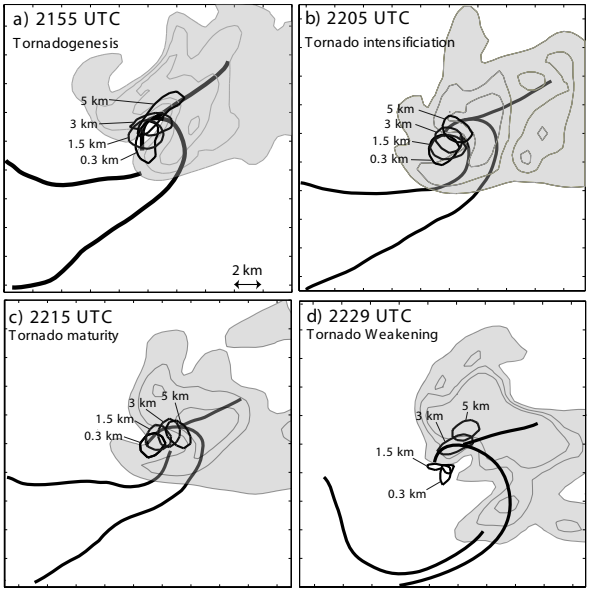

FIG. 4. Ensemble-mean $w = 5$, 10, and 15 m s^{-1} at $z = 5$ km (gray contours and shading), w maximum along the gust fronts near the ground (traced with thick lines), and $\zeta = 0.02$ s^{-1} at 0.3, 1.5, 3.0, and 5.0 km (thin black contours) at four times throughout the life cycle of the tornado.

level convergence and a strengthening or steady circulation, at least at small scales.

Prior to tornadogenesis, the low-level mesocyclone is more negatively buoyant than during intensification, during which, low-level buoyancy slightly increases (Fig.5b). However, the mesocyclone becomes slightly more negatively buoyant as the tornado reaches maturity. The outflow air is the most dense during the weakening stage of the tornado. The greatest cooling approximately corresponds to the development of azimuthally-averaged divergence (Fig.5a) and the enlargement of the RFD maximum near the vertical vorticity maximum (Fig.3e). The evolution of convective available potential energy (CAPE), convective inhibition (CIN), and level of free convection (LFC) of parcels surrounding the mesocyclone center are shown in Fig.5c-d. These sounding indices are calculated by first modifying the base-state sounding at z = 200 m with the ensemble-mean T and T_d located at 20 points along a 2-km-wide ring centered on the vertical vorticity maximum. Each of the 20 parcels are then lifted pseudoadiabatically from z = 200 m to obtain the CAPE, CIN, and LFC (if an LFC exists), which are averaged for the fraction of the 20 parcels that have an LFC at each time. The fraction of parcels containing LFCs are shown in Fig.5d. The cooling of the low-level mesocyclone corresponds to a decreasing average CAPE (ΔCAPE $\sim$ - 500 J kg^{-1}), increasing CIN (ΔCIN $\sim$ 60 J kg^{-1}), and a rise in LFC (ΔLFC $\sim$ 250 m) among parcels surrounding the tornado that have an LFC. Furthermore, fewer parcels contain LFCs as the tornado begins to weaken, decreasing from 100% during tornadogenesis to roughly 60% near tornado demise. The greatest of these changes occurs during tornado maturity. These calculations suggest that decreasing buoyancy in the mesocyclone is making it difficult for parcels to be lifted up to their LFCs (if

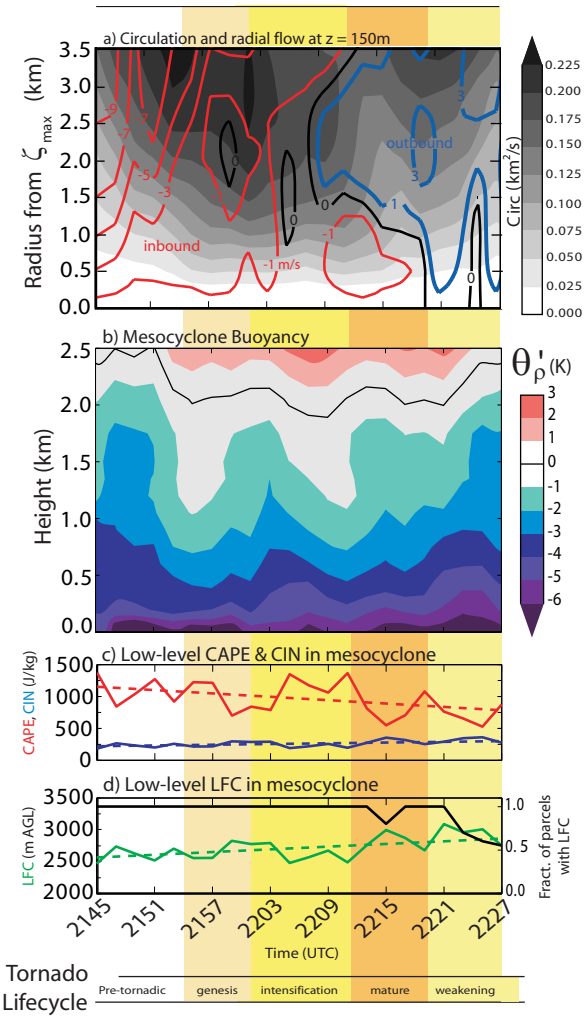

FIG. 5. a) Circulation (shaded) and radial velocity (contours) with respect to the vertical axis of rotation at z = 150 m as a function of time and radius from the axis. b) Ensemble-mean density potential temperature deficit from the environment averaged within a 3-km-diameter circle centered on the maximum of ζ as a function of height and time. c) Evolution of the average CAPE and CIN surrounding the low-level mesocyclone. d) Same as panel c, but LFC and the fraction of the parcels that have an LFC.

they exist), reducing the low-level mesocyclone-scale convergence surrounding the tornado.

4. Trajectory analysis

The flow through the low-level mesocyclone during the formation and weakening stages of the tornado is illustrated with trajectory calculations in Fig.6. Forward- and backward-integrated trajectory calculations are performed using the ensemble mean u, v, and w analyses available every two minutes with a 20-s time step. Most parcels entering the low-level mesocyclone at both times approach the mesocyclone from the northeast through the baroclinic zone on the forward flank of the storm. These trajectories are qualitatively similar to several

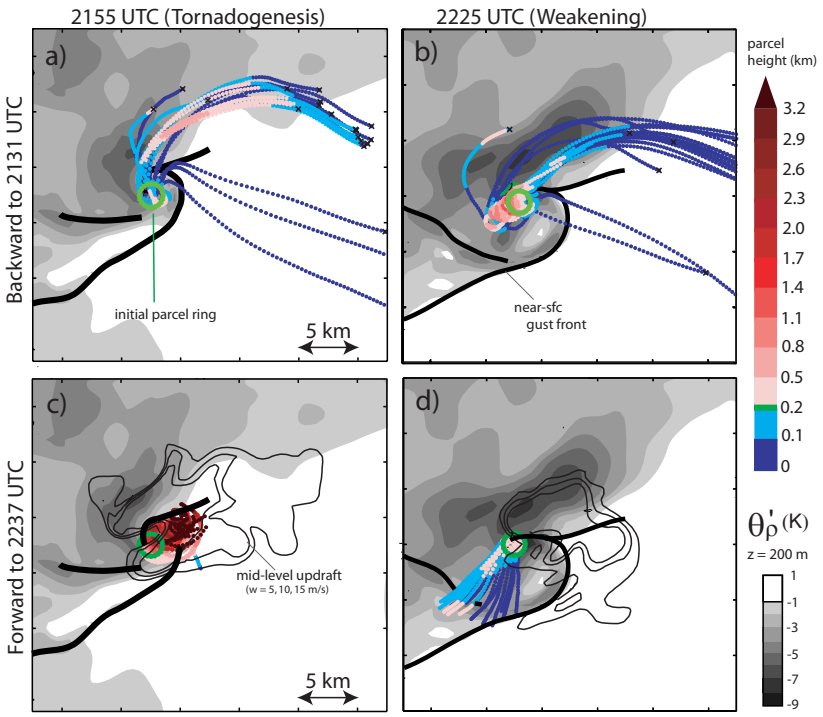

FIG. 6. Top) Backward (in time) trace of 20 parcel trajectories surrounding the maximum of ζ at z = 200 m during (a) tornadogenesis and (b) tornado demise. Parcels are initially located 1 km from the maximum of ζ (green dots). Dots along the trajectories are colorized according to parcel altitude above the ground level and are overlaid on ensemble-mean density potential temperature deficit (shaded) and the near-surface gust front positions (thick black lines) at 2155 and 2225 UTC. Trajectories are traced back in time to 2131 UTC. c and d) Same as in panels a and b, but for parcel trajectories integrated forward in time to 2237 UTC. Ensemble-mean w = 5, 10, and 15 m s^{-1} at z = 5 km are shown with black contours.

studies using limited observations or numerical simulations of supercell thunderstorms. A few parcels enter the mesocyclone more directly from the inflow environment, passing through the inflow notch north of the axis of rotation. It is possible that these trajectories are an artifact of inadequate temporal resolution of the analyses (Dahl et al. 2012).

A comparison of the backward trajectories entering the mesocyclone at each time indicates no significant changes in the paths taken by both groups of parcels (Fig.6a,b). Perhaps one noteworthy difference at these two times is that parcels surrounding the tornado during its demise descend to their positions along the ring at z = 200 m as they circulate within the mesocyclone. They subsequently spread horizontally into the low-level rear-flank outflow. Conversely, the majority of the parcels surrounding the mesocyclone during tornadogenesis ascend into the primary updraft as they circulate within the mesocyclone. This trend is consistent with the increasing near-surface divergence and decreasing buoyancy of the outflow surrounding the tornado as it matures and weakens (Fig.5).

Past studies have indicated that the tilting of horizontal vorticity produced from baroclinic generation in the forward flank of the storm is a primary source of vertical vorticity for the low-level mesocyclone. Subsequent stretching can modify vertical vorticity to mesocyclone or tornado intensity. The magnitude of the baroclinically-generated horizontal vorticity calculated along the trajectories of the parcels that traverse the forward flank and enter the mesocyclone using,

$$\omega_{bc} = \left| \int \left(\nabla \times B\hat{k} \right) dt \right|, \tag{1}$$

where $B = g\frac{\theta_\rho - \overline{\theta_\rho}}{\overline{\theta_\rho}}$, θ_ρ is the ensemble-mean density potential temperature of the parcel (Emanuel 1994), and $\overline{\theta_\rho}(z)$ is the environmental density potential temperature, is shown in Fig.7. Parcels with the largest ω_{bc} enter the mesocyclone just prior to the formation of and during the demise of the tornado. Parcels entering the low-level mesocyclone during the intensification stage of the tornado contain the lowest ω_{bc}. The tilting of horizontal vorticity into the vertical is greatest during the tornadogenesis stage and generally decreases throughout the remainder of the tornado life cycle (Fig.7b). These observations suggest that even though a larger amount of ω_{bc} was available to be tilted during tornado dissipation than during tornadogenesis and intensification, the disruption of the low-level updraft-downdraft structure surrounding the low-level mesocyclone disrupts the tilting mechanism such that anticyclonic vorticity is generated. This trend is consistent with a decreasing supply of cyclonic vertical vorticity produced along parcel trajectories that can be subsequently stretched into mesocyclone or tornado strength. Several studies have indicated the dominance of the stretching term in the vertical vorticity equation at low-levels surrounding tornadoes. Though it is difficult to quantitatively evaluate the stretching of vertical vorticity of individual parcels within the mesocyclone in this case owing to potentially large trajectory errors in this re-

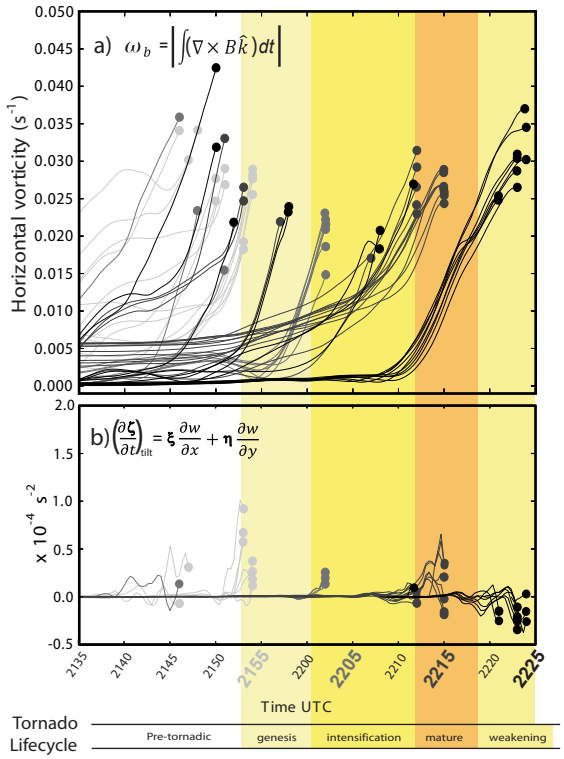

FIG. 7. Top) Magnitude of the horizontal vorticity vector produced by baroclinic generation along trajectories traversing the forward-flank region en route to positions surrounding the mesocyclone center at four times, 2155, 2205, 2215, and 2225 UTC. The calculations for the 2155 and 2225 UTC parcels (lightest gray and black lines, respectively) are performed along the trajectories shown in Fig.6a,b that traverse the forward-flank. The two sets of darker gray lines are calculations performed along forward-flank trajectories of parcels that end up at similar positions relative to the mesocyclone center but at 2205 and 2215 UTC. The calculations are terminated along the trajectories when each parcel acquires ζ = 0.01 s^{-1} (indicated with dots). Bottom) The values of instantaneous tilting of horizontal vorticity into the vertical as a function of time along the same parcel trajectories shown above. The pre-tornadic through weakening stages of the tornado are labeled at the bottom of the figure.

gion, azimuthally-averaged radial divergence at $r > 1$ km after 2205 UTC (Fig.5a) suggests that cyclonic vertical vorticity produced by tilting is weakened on the mesocyclone-scale by negative stretching. This trend is perhaps consistent with the increased ω_{bc} near the end of the tornado life cycle owing an increased horizontal baroclinic gradient associated with colder outflow air present in the forward-flank region (Fig.3e) that enters the mesocyclone during tornado demise and possibly disrupts the low-level updraft-downdraft structure. However, because the tornado reaches maturity after the development of mesocyclone-scale divergence, positive tilting and stretching at spatial scales smaller than that resolved by a 500-m model grid may be responsible for the intensification and maintenance of the tornado after it has formed.

The disconnect between the midlevel updraft and the low-level updraft near the mesocyclone during tornado demise is further illustrated with backward-integrated trajectories of parcels located within the midlevel updraft (Fig.8). Although parcels entering the midlevel updraft have similar origins throughout the life cycle of the tornado, the paths traversed by parcels located within the midlevel mesocyclone differ. During the formation and intensification of the tornado, air passing through the midlevel mesocyclone ascends from the inflow environment and from within the negatively buoyant low-level mesocyclone. However, during the mature and weakening stages of the tornado, air ascends up the rear-flank gust front into the midlevel mesocyclone from the inflow environment rather than from within the low-level mesocyclone and outflow air. In addition to highlighting the developing disconnect between sources of air comprising the low- and midlevel mesocyclone, this analysis indicates that even though the low-level updraft surrounding the dying tornado weakens, the midlevel updraft and rotation survive by directly drawing upon air from the inflow environment.

5. Rear-flank downdraft origins

The importance of the evolution of the rear-flank downdraft on the mesocyclone and tornado life cycle commands a diagnosis of the origins of the descent in this storm. To perform this task we trace trajectories of parcels located at model grid points where the ensemble mean $w < 1$ m s^{-1} at z = 200 m AGL within the downdraft maxima near the tornado shown in Fig.3b and e. Certain trajectories representing many neighboring trajectories in these downdrafts are shown in Fig.9. Parcels located in the downdraft located northwest-west of the developing tornado ascend in the forward flank from a variety of altitudes between 250-1600 m AGL in the inflow environment (these heights may differ if the backward trajectories were calculated beyond 2131 UTC) and finally descend to z = 200 m AGL northwest of the mesocyclone center (e.g., parcels 1 and 2 Fig.9a). These parcels are approximately neutrally buoyant leading up to their ascent and become negatively buoyant just prior to their descent (parcels 1 and 2 Fig.9c). Parcels within the downdraft maximum just southeast of the developing tornado contain somewhat different trajectories and buoyancy characteristics. These parcels approach the downdraft maximum from lower altitudes and circulate within the mesocyclone (e.g., parcel 3 in Fig.9a). They ascend while quite negatively buoyant (e.g., -10 $< t <$ -5 min in Fig.9c), which may imply that significant upward-directed vertical perturbation pressure gradient forces (hereafter VPPGFs) affect their ascent at this time.

The parcels within the large near-surface downdraft just south of the mesocyclone center during tornado demise contain a mix of the two flow patterns shown above. Trajectories passing through the southeastern half of this downdraft area (e.g., parcel 4 in Fig.9b,d) resemble those of parcels 1 and 2, and trajectories passing through the northwestern half, closer to the vorticity maximum (e.g., parcel 5) resemble those of parcel 3. The relatively strong negative buoyancy of most of these parcels during their ascent, particularly the northwestern most ones, again implies that significant upward-directed VPPGFs influence the vertical motion within the mesocyclone. It is possible that downward-directed VPPGFs could enhance downward motion of these parcels (or near-zero VPPGFs could allow strong negative buoyancy to dominate the downward ac-

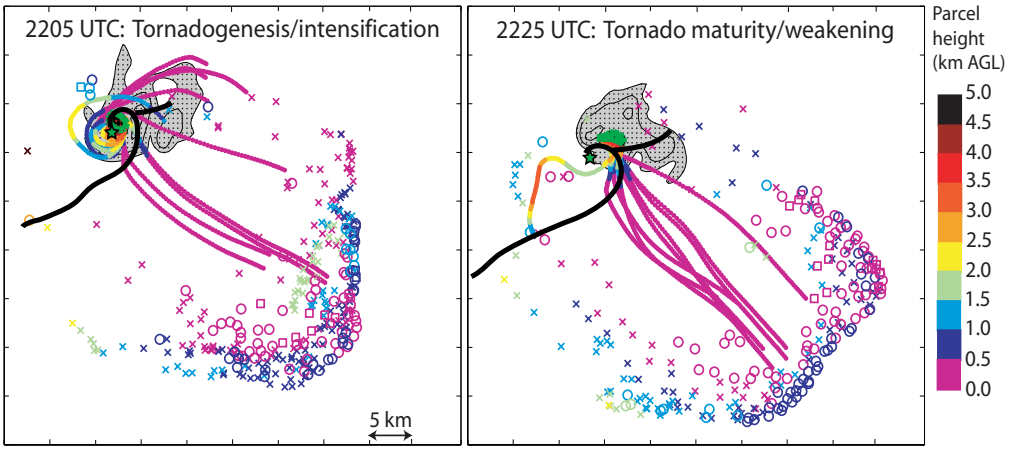

FIG. 8. Analysis of the origin of parcels located at each model grid point at z = 5 km where ensemble-mean $w > 10$ m s^{-1} (fine black dots) integrated backward in time 30 minutes from times representative of (left) tornadogenesis/intensification and (right) tornado maturity/weakening. X's, circles, and squares denote the original positions of parcels that terminate at grid points where 10 m s^{-1} $< w <$ 20 m s^{-1}, 20 m s^{-1} $< w <$ 30 m s^{-1}, and $w >$ 30 m s^{-1}, respectively. These markers are colorized according to parcel altitude. Trajectories of parcels that terminate at grid points where $\zeta > 0.02$ s^{-1} at z = 5 km (thick green contour; representative of the midlevel mesocyclone) are traced throughout the trajectory integration period with dots that are colorized according to parcel altitude. Ensemble-mean w = 10, 20, and 30 m s^{-1} are shown with thin black contours and $w > 10$ m s^{-1} is shaded in gray. The w maximum along the near-surface gust fronts are traced with thick black lines and the near-surface ζ maximum is located with a green star.

celeration). Nevertheless, the apparent merger of these possible downdraft forcings near the tornado at this time disrupts the low-level updraft stucture that was once favorably-arranged for tornadogenesis and maintenance.

6. Summary and Conclusions

This paper outlines an analysis of the Goshen County, Wyoming, tornadic supercell performed using the results of numerical simulations that assimilate mobile radar velocity observations collected during VORTEX2. We focus on understanding certain storm-scale and mesocyclone-scale processes that might affect the formation, maintenance, and dissipation of the tornado that cannot be adequately evaluated by only the dual-Doppler and in situ observations.

The formation and intensification of the tornado occurs underneath the midlevel updraft while the CAPE (CIN and LFC) of parcels in the low-level mesocyclone is (are) relatively high (low), and the low-level horizontal convergence and updraft nearby is relatively strong. These properties promote the ascent of outflow air located within the low-level mesocyclone into the main updraft, yielding the inward advection (relative to the axis of rotation) of near-surface angular momentum. The low-level updraft and downdraft structure within the storm promotes a favorable tilting of horizontal vorticity into the vertical that could be subsequently stretched to mesocyclone or tornado strength.

Changes in certain attributes of the low-level outflow cause the tilting and stretching mechanisms on the rear flank of the storm to become less supportive of the mesocyclone during tornado maturity and demise. A drop (rise) in CAPE (CIN and LFC) occur while the RFD intensifies and becomes larger near the mesocyclone center. These changes correspond to decreasing low-level horizontal convergence within the mesocyclone. The trajectories of parcels that pass through the midlevel mesocyclone during tornado maturity and demise do not pass through the low-level (tornado-containing) mesocyclone as they did during tornadogenesis and intensification. This fact, along with a more tilted mesocyclone structure present at these times, may imply that negativel buoyant outflow diminishes the lift of low-level outflow air near the tornado.

Acknowledgments. This research was funded by NSF grants: AGS–0801035, AGS–0801041, and AGS-1157646, ATM-1211131, ATM-0801041, and NOAA's Warn-on-Forecast project. The DOW radars are NSF Lower Atmospheric Observing Facilities supported by ATM-0734001. Data assimilation experiments were conducted on NCAR CISL supercomputing facilities using the NCAR Data Assimilation Research Testbed and WRF-ARW software packages. We would like to thank Glen Romine, Lou Wicker, Chris Snyder, George Bryan, Jeff Anderson, Dan Dawson, Robin Tanamachi, Hugh Morrison, Nancy Collins, Don Burgess, Matt Parker, and Morris Weisman for advice and helpful discussion of topics related to this research. We also are thankful to all participants of VORTEX2 for their dedication in collecting the data used in this study.

REFERENCES

Anderson, J., T. Hoar, K. Raeder, H. Liu, N. Collins, R. Torn, and A. Avellano, 2009: The Data Assimilation Research Testbed: A community facility. *Bull. Amer. Meteor. Soc.*, **90**, 1283–1296.

Dahl, J.M., M.D. Parker, and L.J. Wicker, 2012: Uncertainties in trajectory calculations within near-surface mesocyclones of simulated supercells. *Mon. Wea. Rev.*, **140**, 29592966.

Dowell, D. C., and H. B. Bluestein, 2002: The 8 June 1995 McLean, Texas, storm. Part II: Cyclic tornado formation, maintenance, and dissipation. *Mon. Wea. Rev.*, **130**, 2649-2670.

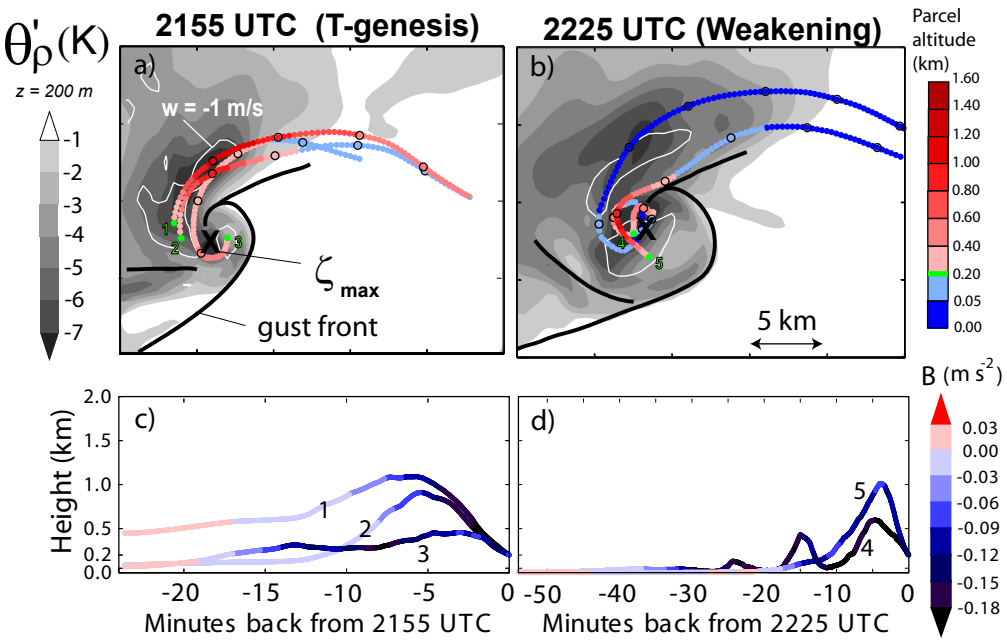

FIG. 9. a and b) Same as Fig.6 except for certain parcels located within the rear-flank downdraft at z = 200 m. The w = -1 m s^{-1} value is shown with a white contour. Small black rings along each trajectory mark 5-min increments back from the initial parcel location (green dots). An 'X' denotes the location of the vetical vorticity maximum at z = 200 m. c and d) Parcel altitude as a function of time. Each trace is colorized according to the vertical acceleration of the parcel due to buoyancy.

Dowell, D.C., and L.J. Wicker, 2009: Additive noise for storm-scale ensemble data assimilation. *J. Atmos. Oceanic Technol.*, **26**, 911–927.

Emanuel, K.A., 1994: *Atmospheric convection.* Oxford University Press.

Finley, C., B. Lee, C. Karstens, M. Grzych, and T.M. Samaras, 2010: Mobile mesonet observations of the rear-flank downdraft evolution associated with a violent tornado near Bowdle, SD on 22 May 2010. Preprints, *25th Conf. On Severe Local Storms*, Denver, CO, Amer. Meteor. Soc., 8A.2.

Kosiba, K., J. Wurman, Y. Richardson, P. Markowski, P. Robinson, and J. Marquis, 2012: Genesis of the Goshen, County, Wyoming tornado on 05 June 2009 during VORTEX2. *Mon. Wea. Rev.*, doi: 10.1175/MWR-D-12-00056.1.

Lemon, L. R., and C. A. Doswell, 1979: Severe thunderstorm evolution and mesocyclone structure as related to tornadogenesis. *Mon. Wea. Rev.*, **107**, 1184-1197.

Lin, Y., R.D. Farley, H.D. Orville, 1983: Bulk parameterization of the snow field in a cloud model. *J. Appl. Meteor.*, **22**, 1065–1092.

Markowski P. M., 2002: Hook echoes and rear-flank downdrafts: A review. *Mon. Wea. Rev.*, **130**, 852–876.

Markowski P., M. Majcen, Y. Richardson, J. Marquis, and J. Wurman, 2011: Characteristics of the wind field in a trip of nontornadic low-level mesocyclones observed by the Doppler on Wheels radars. *Electronic J. Severe Storms Meteor.*, **5** (7), 1–24.

Markowski P. M., Y. Richardson, J. Marquis, J. Wurman, K. Kosiba, P. Robinson, D. Dowell, E. Rasmussen, R. Davies-Jones, 2012a: The pretornadic phase of the Goshen County, Wyoming, supercell of 5 June 2009 intercepted by VORTEX2. Part I: Evolution of kinematic and surface thermodynamic fields. *Mon. Wea. Rev.*, **140**, 28872915

Markowski P. M., Y. Richardson, J. Marquis, J. Wurman, K. Kosiba, P. Robinson, E. Rasmussen, and D. Dowell, 2012b: The pretornadic phase of the Goshen County, Wyoming, supercell of 5 June 2009 intercepted by VORTEX2. Part II: Intensification of low-level rotation. *Mon. Wea. Rev.*, **140** 29162938.

Marquis J., Y. Richardson, P. Markowski, D. Dowell, and J. Wurman, 2012: Tornado maintenance investigated with high-resolution dual-Doppler and EnKF analysis. *Mon. Wea. Rev.*, **140**, 3–27.

Palmer, R., M.I. Biggerstaff, P. Chilcon, G. Zhang, M. Yeary, J. Crain, T. Yu, Y. Zhang, K. Droegemeier, Y.Hong, A. Ryzhkov, T. Schuur, S. Torres, 2009: Weather Education at the University of Oklahoma – An integrated approach. *Bull. Amer. Meteor. Soc.*, **90**, 1277–1282.

Richardson, Y., P. Markowski, J. N. Marquis, J. Wurman, K. A. Kosiba, P. Robinson, D. W. Burgess, and C. C. Weiss, 2012: Tornado maintenance and demise in the Goshen County, Wyoming supercell of 5 June 2009 intercepted by VORTEX2. Preprints, *26th Conf. On Severe Local Storms*, Nashville, TN, Amer. Meteor. Soc.

Skamarock, W.C., J.B. Klemp, J. Dudhia, D.O. Gill, D. M. Barker, W. Wang, and J.G. Posers, 2008: A description of the advanced research WRF version 3. NCAR Tech. Note TN-468+STR, 88 pp.

Straka, J.M., E.N. Rasmussen, and S.E. Fredrickson, 1996: A mobile mesonet for finescale meteorological observations. *J. Atmos. Oceanic Technol.*, **13**, 921–936.

Waugh, S., and S.E. Fredrickson, 2010: An improved aspirated temperature system for mobile meteorological observations, especially in severe weather. Preprints, *25th Conf. On Severe Local Storms*, Denver, CO, Amer. Meteor. Soc.

Wurman, J., J. M. Straka, E. N. Rasmussen, M. Randall, and A. Zahrai, 1997: Design and deployment of a portable, pencil-beam, pulsed, 3-cm Doppler radar. *J. Atmos. Oceanic Technol.*, **14**, 1502-1512.

Wurman, J., K. Kosiba, P. Markowski, Y. Richardson, D. Dowell, P. Robinson 2010: Finescale single- and dual-Doppler analysis of tornado intensification, maintenance, and dissipation in the Orleans, Nebraska, supercell *Mon. Wea. Rev.*, **138**, 4439–4455.

Wurman, J., D. Dowell, Y. Richardson, P. Markowski, E. Rasmussen, D. Burgess, L. Wicker, H. Bluestein, 2012: The second verification of the origins of rotation in tornadoes experiment: VORTEX2. *Bull. Amer. Meteor. Soc.*, /bf 93, 1147–1170.